Palladium at high pressure and high temperature: A combined experimental and theoretical study

Baty, Samuel R.
Burakovsky, Leonid
Luscher, Darby Jon
Anzellini, S.
Errandonea, D.

To be published in: Journal of Applied Physics

DOI to publisher's version: 10.1063/5.0179469

RESEARCH ARTICLE | FEBRUARY 16 2024

Palladium at high pressure and high temperature: A combined experimental and theoretical study

S. R. Baty ; L. Burakovsky ; D. J. Luscher ; S. Anzellini ; D. Errandonea

J. Appl. Phys. 135, 075103 (2024)
https://doi.org/10.1063/5.0179469

Journal of Applied Physics | ARTICLE | pubs.aip.org/aip/jap

Palladium at high pressure and high temperature: A combined experimental and theoretical study

Cite as: J. Appl. Phys. **135**, 075103 (2024); doi: 10.1063/5.0179469
Submitted: 2 October 2023 · Accepted: 11 January 2024 ·
Published Online: 16 February 2024

View Online Export Citation CrossMark

S. R. Baty,[1] L. Burakovsky,[1,a)] D. J. Luscher,[1] S. Anzellini,[2,3] and D. Errandonea[3]

AFFILIATIONS

[1]Los Alamos National Laboratory, Los Alamos, New Mexico 87545, USA
[2]Diamond Light Source Ltd., Diamond House, Harwell Science Campus, Didcot, Oxfordshire OX11 0DE, UK
[3]Departamento de Física Aplicada-ICMUV, MALTA Consolider Team, Universidad de Valencia, Edificio de Investigación, C/Dr. Moliner 50, Burjassot, Valencia 46100, Spain

[a)]**Author to whom correspondence should be addressed:** burakov@lanl.gov

ABSTRACT

Palladium is one of the most important technological materials, yet its phase diagram remains poorly understood. At ambient conditions, its solid phase is face-centered cubic (fcc). However, another solid phase of Pd, body-centered cubic (bcc), was very recently predicted in two independent theoretical studies to occur at high pressures and temperatures. In this work, we report an experimental study on the room-temperature equation of state (EOS) of Pd to a pressure of 80 GPa, as well as a theoretical study on the phase diagram of Pd including both fcc-Pd and bcc-Pd. Our theoretical approach consists in *ab initio* quantum molecular dynamics (QMD) simulations based on the Z methodology which combines both direct Z method for the simulation of melting curves and inverse Z method for the calculation of solid–solid phase transition boundaries. We obtain the melting curves of both fcc-Pd and bcc-Pd and an equation for the fcc–bcc solid–solid phase transition boundary as well as the thermal EOS of Pd which is in agreement with experimental data and QMD simulations. We uncover the presence of another solid phase of Pd on its phase diagram, namely, random hexagonal close-packed (rhcp), and estimate the location of the rhcp-bcc solid–solid phase transition boundary and the rhcp–fcc–bcc triple point. We also discuss the topological similarity of the phase diagrams of palladium and silver, the neighbor of Pd in the periodic table. We argue that Pd is a reliable standard for shock-compression studies and present the analytic model of its principal Hugoniot in a wide pressure range.

INTRODUCTION

Palladium (Pd) is one of the least studied transition metals. It has the lowest ambient melting point and mass density of all the six platinum group metals (Ru, Os, Rh, Ir, Pd, Pt). It is soft and ductile, and at the same time highly resistant to corrosion and scratching. Because of its excellent hydrogen absorption capacity, palladium is used in the fields of electronic information technology and medical device manufacturing. In fact, Pd exhibits a number of exceptional properties which enable its application in a myriad of hydrogen technologies. Indeed, Pd is the only d-electron transition metals which has all of its electron shells completely filled; its electron shell configuration is $[^{36}Kr]\ 4d^{10}$. Hence, on the outer layer of the Pd atom, unlike Pt and other d-electron transition metals, there are no outer electrons (the s and p orbitals are empty), so it has many easily accessible vacancies to be filled by hydrogen atoms. Because of this, Pd has the ability to absorb large volumetric quantities of hydrogen at room temperature (T) and atmospheric pressure (P), and subsequently forms palladium hydride (PdH_x) which exhibits the noble character of Pd.[1] In fact, Pd can absorb hydrogen in a volume ratio of up to $\sim 1:1000$ which corresponds to $x \sim 0.7$ in the above structure formula. Since x increases with increasing P, and $x = 1$ eventually occurs at high enough P[2] or can be achieved by electrochemical methods,[3] it is extremely important to have the accurate knowledge of the high-P properties of Pd including its phase diagram.

However, the vast majority of studies on Pd have so far focused on its properties at ambient P,[4–6] and very little is known about its properties under extreme conditions, and its phase diagram is poorly understood. At normal P, Pd is a typical face-centered cubic (fcc) metal, and its fcc structure remains stable up to its ambient melting point (T_m). To the best of our knowledge, only four experimental studies on the equation of state (EOS) of Pd have been published up-to-date,[2,7–9] one of them in relation to the calibration of the ruby pressure gauge,[7] which all demonstrate the structural stability of fcc-Pd to a pressure of 182 GPa.[9] Hence, Pd could have potentially been used as a pressure calibrant in high-P experiments as well as a shock standard in shock compression experiments provided that its structural stability is confirmed experimentally and both its phase diagram and EOS are known. We note, however, that the high hydrogen affinity of Pd may be a large drawback in its practical application as a pressure marker since hydrogen trace contamination which is very hard to detect will cause changes in the ambient pressure density. This has been suggested as a potential reason for the discrepancy in current experimental EoSs.[9]

Nonetheless, both the high-P thermodynamic and structural properties of Pd remain poorly understood. A recent theoretical study[10] reveals a structural solid–solid phase transition in shock-compressed palladium, from the ambient fcc to the high-PT body-centered cubic (bcc) solid phase. A similar fcc–bcc solid–solid phase transition under shock occurs in both copper[11,12] and silver,[11,13] the Pd neighbors of the periodic table. More recent independent theoretical study[14] results in the phase digram of Pd having both ambient fcc and high-PT bcc solid phases such that the location of the fcc–bcc solid–solid phase boundary is consistent with the fcc–bcc transition point on the Pd Hugoniot from Ref. 10.

It is important to confirm the existing results on the EOS and phase diagram of Pd in both experimental and independent theoretical studies. It is also important to extend our current knowledge of the melting curve of Pd which has so far been measured in only one experimental study to 30 GPa,[15] and very few theoretical studies of Pd melting at high P are available.[16–19] A combined experimental and independent theoretical study aimed at both confirming the existing experimental results and extending our knowledge of the phase diagram of Pd to much higher pressures is the focus of our present work.

EXPERIMENTAL STUDY

For our experimental study of the room-T EOS of Pd, we used a membrane diamond anvil cell (DAC) with diamonds of 150 μm culets beveled to 300 μm. We used a Re gasket with He as a pressure medium. The pressure was determined from a W marker following the calibration of Dewaele *et al.*[20] Pd in powder form was obtained from Goodfellow (99.9% purity). Angular-dispersive powder x-ray diffraction (XRD) patterns were collected at the extreme conditions beamline, I15,[21] of the Diamond Light Source, using a monochromatic beam (29.5 keV) focused down to $6 \times 9\,\mu\text{m}^2$. A Pilatus 2M detector was used for data collection. The sample-to-detector distance was measured following the standard procedure from the diffraction rings of CeO_2 and appeared to be around 430 mm. In order to extract the diffraction signal from the sample, masks were applied on a per-image basis, and the images were azimuthally integrated using the DIOPTAS suite.[22] A Pawley refinement of the patterns obtained was performed with the TOPAS suite[23] using the previously reported parameters as the starting values.

The XRD patterns at selected pressures obtained in our experimental study are shown in Fig. 1. Up to the highest pressure

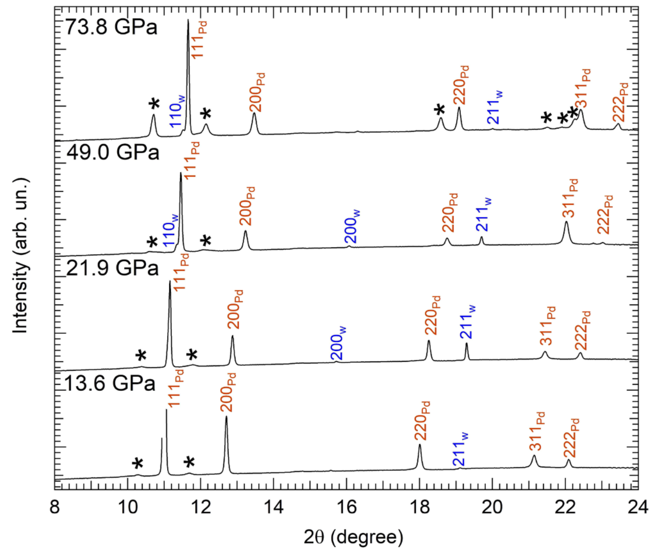

FIG. 1. XRD patterns at selected pressures collected in our experiments using a monochromatic wavelength of 0.420 28 Å (energy of 29.5 keV). The Pd (fcc) and W (bcc) peaks are marked with the corresponding subscripts, and those from Re (hcp) gasket with asterisks.

measured in the experiment (~ 80 GPa), the Pd peaks can be indexed with the fcc structure. Thus, fcc-Pd appears to be stable up to 80 GPa, in agreement with the previous experiments.[2,7–9] The fcc-Pd unit-cell parameters (lattice constant a and unit-cell volume $V = a^3/4$) were determined as a function of P; $V = V(P)$ can be found in Table S1 of the supplementary material. Then, the corresponding experimental $T = 300$ K EOS was compared to our theoretical calculations described in the following section.

THEORETICAL STUDY

Here is the summary of the theoretical methodology used in our study. The detailed discussion of each of the methods is offered in the following sections of our paper.

Methods

Our theoretical study of the phase diagram of Pd was carried out using VASP (Vienna *Ab initio* Simulation Package).[24,25] The electron core-valence structure of Pd was chosen to be $[^{30}\text{Zn}]\,4p^6\,4d^{10}$, i.e., the 16 outermost electrons of Pd were assigned to the valence. The valence electrons were represented by a plane-wave basis set with a cutoff energy (ENCUT in VASP) of 437.5 eV, while the core electrons were represented by projector augmented-wave (PAW) pseudopotentials. The generalized gradient approximation (GGA) with the revised Perdew–Burke–Ernzerhof (PBEsol) exchange-correlation functional[26] was chosen for our theoretical study. This choice was made based on the detailed analysis of Ref. 27 of the performance of three exchange-correlation functionals GGA-PBE, GGA-PBEsol, and LDA (local density approximation) available in VASP as applied to $3d$, $4d$, and $5d$ transition metals. It was concluded that 3*d* transition metals are best described by GGA-PBE while both 4*d* and 5*d* ones by GGA-PBEsol except, perhaps, iridium and gold which are both described best by LDA. This conclusion has been confirmed in numerous theoretical studies that followed since then, e.g., PBE for Cu,[12] PBEsol for Ag,[13] and LDA for Au,[28] and our present study is no exception. The core radius (the largest value of RCUTs among those for each of the quantum orbitals) of this 16-electron pseudopotential is 2.4 a.u., or 1.27 Å. Since numerical errors in the calculations using VASP remain almost negligible until the nearest neighbor distance reaches $2 \times \text{RCUT}/(1.25 \pm 0.05)$,[29] with this pseudopotential one can study systems with densities up to $\sim 40\,\text{g/cm}^3$ (a pressure of ~ 5 TPa).

1. Cold enthalpies and equations of state

Cold ($T = 0$) enthalpies, $H = E + PV$ (E is energy and V volume) were calculated for the following six different solid structures of Pd over the pressure range 0–2500 GPa: (i) fcc, (ii) bcc, (iii) hexagonal close-packed (hcp); 2 atoms per unit cell, (iv) double-hcp (dhcp); 4 atoms per unit cell, (v) triple-hcp (thcp); 6 atoms per unit cell, and (vi) 9R (α-Sm); 9 atoms per unit cell. The corresponding values of the unit cell lattice constants, their increments, the total number of points, and the *k*-point meshes used in this calculation are listed in Table I.

For hexagonal structures, a is that of the ideal lattice ($c/a = n\sqrt{2/3}$, where n is the number of atoms per unit cell). At each a, the unit cell was first optimized to obtain the corresponding values of a and c of the real unit cell; these real unit cells were used for the calculation of H. With such dense *k*-point meshes, for all the six solid structures full energy convergence to $\tilde{<}1$ meV/atom is achieved in the entire P range. An example of the convergence test for fcc-Pd with a lattice constant of 2.86 Å (the corresponding P is ~ 1.9 TPa) in terms of both E and P as functions of the value of ENCUT shown in Table S2 of supplementary material demonstrates exactly that.

2. Melting simulations

Our quantum molecular dynamics (QMD) melting simulations were carried out using the (direct) Z method implemented with VASP which is described in detail in Refs. 30–32. We used a 500-atom ($5 \times 5 \times 5$) supercell for fcc-Pd and a 686-atom ($7 \times 7 \times 7$) supercell for bcc-Pd with a single Γ-point in either case; with such large supercells, full energy convergence, to $\tilde{<}1$ meV/atom, was achieved in every case considered. A time step of 1 fs was used for fcc-Pd and 2 fs for bcc-Pd. The reasons for choosing a much large supercell and a large time step for bcc-Pd are discussed below. We simulated six melting points of each of fcc-Pd and bcc-Pd, by performing an average of five computer runs per point (for a total of ~ 60 computer runs for both structures). For fcc-Pd, the total simulation length was 10000–20000 time steps, while for bcc-Pd 5000–10000, so that the maximum total simulation time was 20 ps in either case.

TABLE I. Numerical values of intervals of the unit cell lattice constants (a), their increments (Δ), the total number of points (N), and the *k*-point meshes used for the calculation of the cold enthalpies of six different solid structures of Pd.

Solid structure	Interval of a (Å)	Δ (Å)	N	k-point mesh
fcc	2.80–4.00	0.075	17	$60 \times 60 \times 60$
bcc	2.20–3.10	0.05	19	$75 \times 75 \times 75$
hcp	1.95–2.80	0.05	18	$80 \times 80 \times 50$
dhcp	1.95–2.80	0.05	18	$100 \times 100 \times 30$
thcp	1.95–2.80	0.05	18	$100 \times 100 \times 20$
9R	1.95–2.80	0.05	18	$110 \times 110 \times 15$

3. Solidification simulations

Our QMD solidification simulations were carried out using the inverse Z method implemented with VASP which is described in detail in Ref. 31. We used a computational cell of 512 atoms prepared by melting a $8 \times 8 \times 8$ solid simple cubic (sc) supercell which was chosen in order to eliminate any (geometric) bias towards solidification into fcc or bcc, or any other solid structure. We used sc unit cells of 2.1, 2.0, 1.95 and 1.85 Å; the corresponding Ps are, respectively, ~ 300, 600, 800 and 1450 GPa. Our *NVT* simulations were carried out using the Nosé-Hoover thermostat with a timestep of 1 fs. The solidification Ts were chosen from 2500 to 7500 K for the 2.1 Å, from 2500 to 12 500 for the 2.0 Å, and from 2500 to 15 000 K for the 1.95 Å supercells, with an increment of 2500 K in each case, and from 1500 to 6000 K for the 1.85 Å supercell with an increment of 1500 K. Complete solidification typically required 15 000–25000 timesteps, i.e., from 15 to 25 ps.

THEORETICAL RESULTS: $T = 0$

Cold enthalpies of the solid phases of Pd

Figure 2 shows differences between the enthalpies of the other five solid structures and that of fcc-Pd, its ambient solid structure, as functions of P.

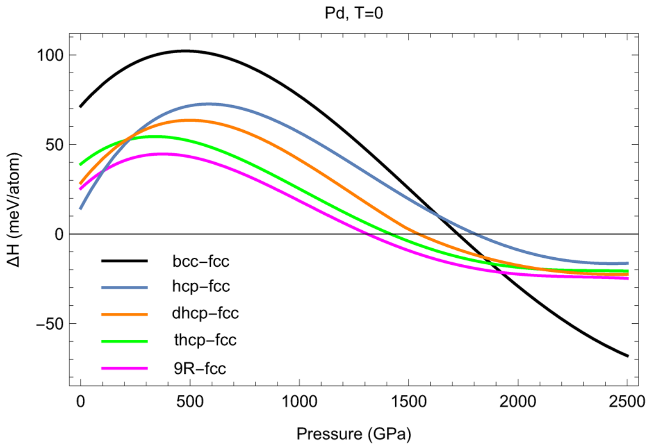

FIG. 2. Differences between the cold enthalpies of five solid structures of Pd and that of fcc-Pd as functions of P.

It is clearly seen that bcc-Pd becomes the ground state of Pd on increasing P; the fcc–bcc transition corresponds to $\sim$ 1700 GPa. This is in agreement with the theoretical study of Ref. 17 which concludes that fcc remains the thermodynamically most stable phase of Pd up to at least 1000 GPa. Figure 2 is very similar to Fig. 2 of Ref. 14 which compares the enthalpies of the other three solid phases of Pd to that of fcc: the fcc–bcc transition corresponds to ∼1900 GPa and the maximum of the bcc-fcc enthalpy difference also occurs at ∼500 GPa and is ∼8 mRy/atom, or ∼110 meV/atom, consistent with our calculations. However, we find three hexagonal polytypes, dhcp, thcp and 9R, which are all more stable than fcc-Pd above $P > 1300$ GPa and are separated from each other by $\sim 5\ \widetilde{\text{meV/atom}}$ only. This may suggest the appearance of random-hcp (rhcp) phase as the ground state of Pd in the pressure interval of ∼1300–1700 GPa which is discussed in more detail in what follows.

Cold equations of state of fcc-Pd and bcc-Pd

Fitting the results on $P = P(V)$ of our cold enthalpy calculations with the third-order Birch–Murnaghan (BM3) EOS of the form [in the following ρ stands for density, in g cm^{-3}, B and B' for bulk modulus, in GPa, and its pressure derivative, and the subscript 0 means ($T = 0,\ P = 0$)]

$$P(\rho) = \frac{3}{2} B_0 \left(\eta^{7/3} - \eta^{5/3}\right)\left[1 + \frac{3}{4}(B_0' - 4)\left(\eta^{2/3} - 1\right)\right], \qquad (1)$$

where $\eta = \rho/\rho_0$, results in the following sets of parameters for the two solid phases:

$$\text{fcc-Pd}: \quad \rho_0 = 12.09, \quad B_0 = 195.0(2.5), \quad B_0' = 5.1(1),$$

$$\text{bcc-Pd}: \quad \rho_0 = 12.00, \quad B_0 = 188.0(2.4), \quad B_0' = 5.1(1).$$

Here the uncertainties in the values of B_0 and B_0' are assigned based on the criterion that variations in these parameters do not move the resulting fit outside of the 2σ interval, where σ is the standard deviation.

In each of the two cases, the BM3 analytic form is expected to be reliable to ∼1 TPa. We note that the two EOSs are very similar to each other as regards the values of their parameters. Our value of ρ_0 for fcc-Pd virtually coincides with the experimental 12.093 g cm^{-3} (a molar volume of 8.800 cm^3/mol),[33] and those of B_0 and B_0' for fcc-Pd are in good agreement with $B_0 = 189$ and $B_0' = 5.23$ from independent theoretical calculations.[17] Note that exactly the same theoretical value of B_0 of 195 GPa was obtained in Ref. 34, and that the corresponding $T = 0$ experimental values (from the direct measurements of the eleastic constants of Pd) are 195.4 GPa[35] and 195.05.[36] Because of temperature reduction, the value of B_0 for the 300 K EOS must be lower than 195 GPa at $T = 0$. The two experimental $T = 300$ K values of B_0 are 193.1[35] and 190.01.[36] In fact, the pairs of values (B_0, B_0') from the papers offering experimental room-T EOSs are (162(2),6.2(9)),[2] (183.8,5.36) (our own best fit to the data of[7]), (157(3),9.9(4)) and (203(3),4),[8] and (189.3(30),5.473(63)) and (197.5(33),4.996(66)).[9] We note that the Vinet functional form of the EOS (which can be

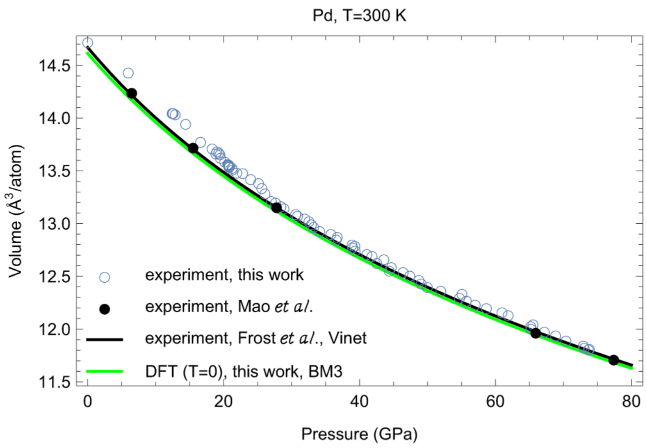

FIG. 3. Comparison of our cold EOS for fcc-Pd (DFT) to the experimental data of both our own (this work) and Ref. 7 (Mao *et al.*) and to the experimental EOS of Ref. 9 (Frost *et al.*) in the Vinet form with $(B_0, B_0') = (189.3, 5.473)$.

found in the supplementary material) was used in,[2] the BM3 one in[7] (our own fit) and,[8] and both the Vinet and BM3 ones in.[9] We also note that our own experimental data in the 0–80 GPa range can be very accurately described by the BM3 form with $V_0 = 14.72(4)$ Å^3/atom (a density of 12.005 g cm^{-3}), $B_0 = 190(3)$ GPa, and $B_0' = 5.3(2)$, consistent with the theoretical values as well as the experimental values of both Refs. 8 and 9 (the results of Ref. 9 cover a much larger P interval than those of Ref. 8).

All the previous experimental room-T EOSs and the theoretical $T = 0$ EOS presented here are compared to each other in Table S3 of the supplementary material. It is clearly seen that up to a pressure of 200 GPa agreement is excellent between all the EOSs except those of Ref. 8. Although the (203(3), 4) EOS of Ref. 8 is slightly stiffer as it predicts $P \sim 170$ GPa at a volume for which the other four predict $P \sim 200$ GPa, the (157(3), 9.9(4)) EOS of Ref. 8 is a clear outlier with the corresponding $P \sim 300$ GPa. This must be related to its unusually high (for transition metals) B_0' value of 9.9.

Figure 3 compares our theoretical cold EOS of fcc-Pd to the experimental points at $T = 300$ K obtained by ourselves in the course of the experimental study described above as well as the five data points of Ref. 7, and to the experimental EOS of Ref. 9 in the Vinet form.

As clearly seen in Fig. 3, agreement between theory and experiment is very good. A small shift of the theoretical curve to the left of the experimental data is because of a small mismatch of volumes that correspond to the same P at $T = 0$ (theory) and $T = 300$ K (experiment) which comes from thermal expansion. With increasing P, this mismatch virtually disappears.

THEORETICAL RESULTS: $T > 0$

"Thermal" equations of state of fcc-Pd and bcc-Pd

The finite-T counterparts of the above two EOSs can be written approximately as

TABLE II. The six *ab initio* melting points of fcc-Pd, (P_m, $T_m \pm \Delta T_m$), obtained from the *Z* method implemented with VASP.

Lattice constant (Å)	Density (g/cm^3)	P_m (GPa)	P_m from (1) and (2)	T_m (K)	ΔT_m (K)
4.00	11.045	−2.60	−2.610	1680	175.0
3.70	13.955	70.8	70.81	4490	175.0
3.45	17.214	225	224.9	8010	312.5
3.25	20.591	492	492.5	12 310	312.5
3.10	23.727	864	863.8	16 890	375.0
3.00	26.180	1252	1252.1	20 860	375.0

$$P(\rho, T) = P(\rho) + \alpha T, \quad \alpha_{\rm fcc} = 6.8 \times 10^{-3}\ {\rm GPa/K}, \quad \alpha_{\rm bcc} = 8.0 \times 10^{-3}\ {\rm GPa/K}. \tag{2}$$

The two values of α in (2) were chosen to match the two ambient melting points the ρ-T coordinates of which are, respectively, (11.18, 1828) from experiment,[33] and (11.24, 1155) from the extrapolation to $P = 0$ of our QMD data on the melting curve of bcc-Pd discussed in what follows.

This form of the thermal EOS does not take into account the T-dependence of the bulk modulus, and/or the P- (or T-)dependence of the thermal expansivity, and is therefore approximate. Yet, it is relatively simple and allows one to easily estimate the value of ρ at the corresponding P and T. For instance, comparison of the values of the melting P (P_m) that these two "thermal EOSs" give while using the corresponding ρs and melting Ts (T_m) to those that come directly from QMD melting simulations clearly demonstrates that Eq. (2) is virtually exact along the melting curves of both fcc-Pd and bcc-Pd. The comparison can be found in Tables I and II. The fact that Eq. (2) is virtually exact along the two melting curves allows one to obtain both densities at the fcc–bcc–liquid triple point and calculate the initial slope of the fcc–bcc transition boundary, which is discussed in more detail below.

Melting curves of fcc-Pd and bcc-Pd

We found out that the use of a 512-atom bcc-Pd supercell (such a supercell was used in our study on the phase diagram of Ag[13]) does not ensure accurate results on the bcc-Pd melting curve, because the corresponding melting simulations exhibit a signature of a mechanical instability, namely, during the QMD runs of bcc-Pd both P and T drift away from ther average values determined by the corresponding P–T conditions of the run. This may be the consequence of the facts that (i) bcc-Pd is mechanically unstable in the range of P considered in this work, and (ii) unless it is fully mechanically stable, a supercell of a size larger than the critical one is required to simulate its thermodynamic behavior correctly. According to Ref. 14, bcc-Pd is mechanically unstable below ~500 GPa at low T and becomes fully mechanically stable in the whole 0-T_m interval of T at $P \gtrsim 600$ GPa. According to Ref. 17, bcc-Pd is mechanically unstable even in a wider range of P, at least up to 800 GPa. The treatment of bcc-Fe of Ref. 37 gives a good example of the critical size of the supercell for the correct description of the temperature-stabilized bcc structure: a supercell of at least 1024-atom ($8 \times 8 \times 8$) is required for bcc-Fe. In our case, such a critical size may be $7 \times 7 \times 7$, since the signature of a mechanical instability disappears for a larger 686-atom ($7 \times 7 \times 7$) supercell which we used for our simulations of bcc-Pd. Since for this supercell the total number of valence electrons exceed 10 000, QMD simulations become extremely time consuming. Hence, a time step of 2 fs was chosen for the simulations of bcc-Pd, compared to 1 fs for those of fcc-Pd, in order to partly offset their computational cost.

The pairs of Figs. 4–7 offer examples of our Z method melting simulations. They correspond to the third of the six T_ms for both fcc-Pd and bcc-Pd, and demonstrate the time evolution of T and P, respectively, during the corresponding computer runs.

Figures 6 and 7 exemplify the behavior of T and P, respectively, during a QMD run. During the entire $T_0 = 20\,875$ K run,

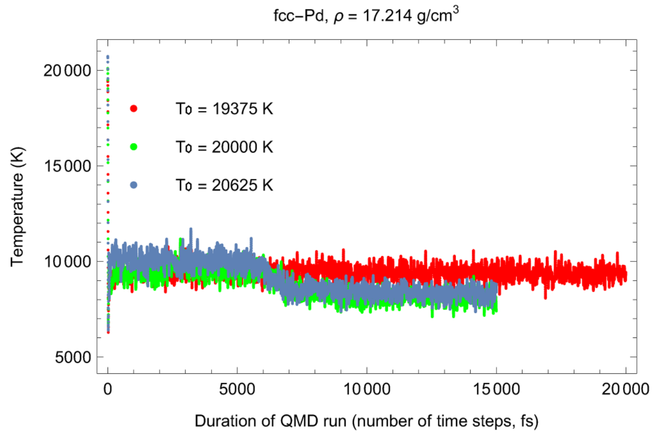

FIG. 4. The melting point (225 GPa, 8010 K) of fcc-Pd at a density of 17.214 g cm^{-3}: melting T from *ab initio* Z method implemented with VASP.

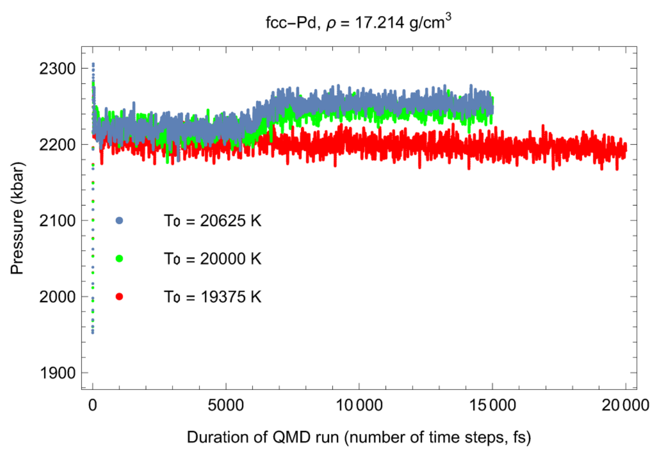

FIG. 5. The same as in Fig. 4 for melting P (in kbar; 10 kbar = 1 GPa).

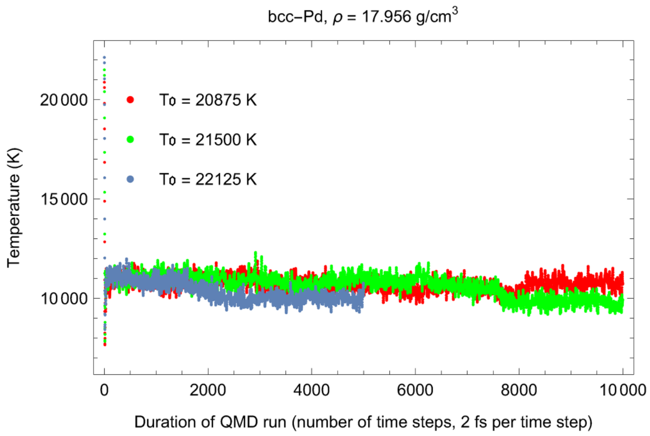

FIG. 6. The melting point (292 GPa, 9850 K) of bcc-Pd at a density of 17.956 g cm^{-3}: melting T from *ab initio* Z method implemented with VASP.

the system remains a superheated solid since during the 20 ps of running time both the average T and P do not change. Melting occurs during the $T_0 = 21\,500$ K run: it starts after $\sim$15 ps of running time and shows up as the decrease of average T from $\sim$11 000 to 9850 K and the corresponding increase of average P from $\sim$290 to 292 GPa; the melting process takes about 2 ps. The simultaneous increase in T and decrease in P happen because during the QMD run the total energy, $E \sim k_B T + PV$, is conserved, and V is fixed. For the same reason, Figs. 6 and 7 appear to be "mirror images" of each other; see Ref. 32 for more detail. In the run with $T_0 = 22\,125$ K, melting starts after 3 ps of running time, but for higher T_0 it will start even faster, sometimes immediately after the beginning of the QMD run.

The results of our melting simulations are summarized in Tables II and III. The errors in melting T (T_m) are half of the

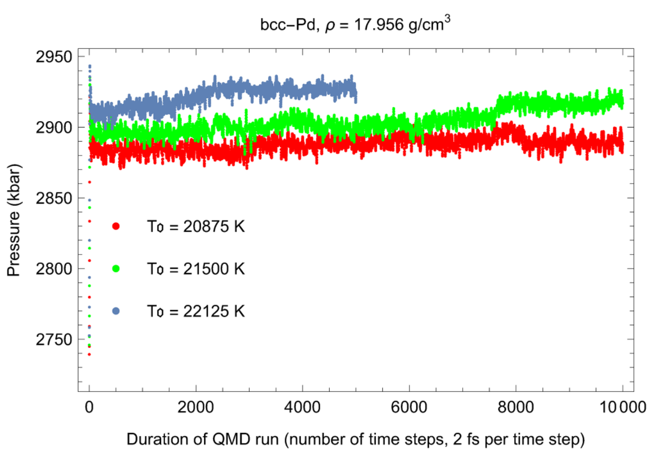

FIG. 7. The same as in Fig. 6 for melting P (in kbar; 10 kbar = 1 GPa).

TABLE III. The six *ab initio* melting points of bcc-Pd, (P_m, $T_m \pm \Delta T_m$), obtained from the Z method implemented with VASP.

Lattice constant (Å)	Density (g/cm^3)	P_m (GPa)	P_m from (1) and (2)	T_m (K)	ΔT_m (K)
3.1	11.864	14.1	14.10	2030	175.0
2.9	14.491	99.2	99.15	5230	175.0
2.7	17.956	292	291.9	9850	312.5
2.6	20.109	471	471.4	13 150	312.5
2.5	22.620	751	750.7	17 480	375.0
2.4	25.567	1189	1189.5	23 190	375.0

increment of the initial T for a series of computer runs at the corresponding density.[32] We chose these increments to be 350 K for the first, 625 K for the second, and 750 K for the third pair of the T_m points in each of the two cases. The corresponding T_m errors are listed in the tables as ΔT_m. The errors in melting P (P_m) are negligibly small, of order 1–2 GPa in each case. Included in Tables II and III are also the values of P_m that come from each of the thermal EOSs (1) and (2) at the corresponding T_ms.

The best fits of the Simon–Glatzel form $T_m(P) = T_m(0)(1 + P/a)^b$ to the six QMD datapoints of Tables II and III represent the corresponding melting curves,

$$T_m^{\text{fcc-Pd}}(P) = 1828 \left(1 + \frac{P}{19.1}\right)^{0.58} \tag{3}$$

and

$$T_m^{\text{bcc-Pd}}(P) = 1155 \left(1 + \frac{P}{9.5}\right)^{0.62}. \tag{4}$$

Both the melting curves (3) and (4) are shown in Fig. 10 below as blue and green lines, respectively.

Since at higher P the melting curve of bcc-Pd is higher than that of fcc-Pd, bcc-Pd is thermodynamically more stable than fcc-Pd and is therefore the actual solid phase of palladium. The two melting curves cross each other at (P in GPa, T in K) $(P, T) = (106.6, 5452)$ which is the fcc–bcc–liquid triple point.

4. Initial slope of the melting curve of Pd

Our value of dT_m/dP at $P = 0$, the initial slope of the melting curve of Pd, comes from Eq. (3): 55.5 K/GPa. It is in the middle of the $\sim$40–64 K/GPa range of the values available the literature: 39.5 (theory,[19]), 45.7 (experiment,[15]), 49.5 (classical MD,[18]), 50 (classical MD,[16]), and 64.0 (theory,[38]); the extremely small value of $\sim$20 K/GPa for the Pd melting curve of Ref. 17 is omitted. It can be compared to the value arising from the Clausius–Clapeyron (CC) formula $dT_m/dP|_{P=0} = T_m \Delta V_m / \Delta H_m$, where ΔV_m and ΔH_m are the molar volume and enthalpy changes at melt, respectively. The literature data on ΔH_m from[4] lie in the range of 16.74–17.46 kJ/mol, i.e., 17.10 ± 0.36 kJ/mol. Arblaster's most recent re-assessment of all the available thermophysical data on Pd available in the literature[6] produced the ΔH_m value of

17.34 ± 0.73 kJ/mol which includes the above range from Ref. 4 and which we adopt for our estimate of the initial slope of the Pd melting curve. The value of ΔV_m from direct experimental measurement of the Pd thermal expansion across T_m is 0.506 cm^3/mol (10.0103 down to 9.5043),[39] while Ref. 40 gives 0.46 cm^3/mol (9.98 down to 9.52). Hence, we adopt $\Delta V_m = 0.483 \pm 0.023\,cm^3$/mol. Finally, $dT_m/dP|_{P=0} = 1828 \times (0.483 \pm 0.023)/(17.34 \pm 0.73) = 51.0 \pm 4.6$ K/GPa, which our value of 55.5 is consistent with at the upper limit.

fcc–bcc solid–solid phase transition boundary in palladium

We now discuss the fcc–bcc solid–solid phase transition boundary in palladium. We start our discussion with the value of its initial slope.

5. Theoretical estimate of the initial slope of the fcc–bcc transition boundary

The similarity of the numerical values of ρ_0, B_0, and B_0' for the two EOSs as well as those of the corresponding αs implies that, in view of the CC formula, if the fcc–bcc phase transition in Pd does occur, at the transition (P, T) the values of the two volumes are expected to be close to each other, thus the corresponding volume change is small, which results in the fcc–bcc phase transition boundary being relatively flat (that is, a variation of T over a wide interval of P is expected to be small and can be well approximated by a horizontal line); in fact, our theoretical phase diagram of Pd shown in Fig. 10 demonstrates that along this phase boundary T varies within ~ 1000 K only over a P range as wide as 1000 GPa.

The formula for the initial slope of a solid–solid phase transition boundary at the solid$_1$–solid$_2$–liquid triple point was derived in our previous work,[13]

$$T_{12}' = \frac{(V_2 - V_1)\, T_1'\, T_2'}{(V_2 - V_1)\, T_1' + \delta\, V_1\, (T_2' - T_1')}, \tag{5}$$

where V_1 and V_2 are, respectively, the volumes of solid$_1$ and solid$_2$ at the triple point, and δ is the volume change at melt of solid$_1$, so that the corresponding liquid volume is $V_\ell = (1+\delta)V_1$. Also, T_1' and T_2' are the slopes of the two melting curves at the triple point (where they cross each other). In the case of Pd, the values of V_1 and V_2 come from the corresponding thermal EOSs, and those of T_1' and T_2' from the corresponding melting curve equations, Eqs. (3) and (4), at $(P, T) = (106.6, 5452)$ of the fcc–bcc–liquid triple point. Specifically, $V_1 = 7.1414\,cm^3$/mol, $V_2 = 7.2547\,cm^3$/mol (i.e., $V_2 > V_1$, thus the phase boundary has a positive slope), and $T_1' = 25.1585$ K/GPa and $T_2' = 29.1171$ K/GPa. It is argued in Ref. 41 that at $P \sim 80$–100 GPa volume change at melt of fcc-Cu decreases by a factor of ~ 2. Assuming that the behavior of $\delta = \delta(P)$ for fcc-Pd is similar to that of fcc-Cu (the same assumption was made in our study of Ag[13] and appeared to be fully justified by comparison to the results of other independent theoretical method), and taking into account that, as discussed above, at $P = 0$ $\delta \simeq 0.05$, we can expect that at the Pd fcc–bcc–liquid triple point $\delta \sim 0.025$. For our estimate of T_{12}' we assume that at the Pd fcc–bcc–liquid triple point $0.02 \le \delta \le 0.03$. Then, Eq. (5) gives $T_{12}' = 23.4 \pm 1.0$ K/GPa. Thus, the initial slope of the fcc–bcc solid–solid phase boundary is $\simeq 23$ K/GPa.

6. Inverse-Z simulations on the P-T location of the fcc–bcc transition boundary

The above discussions of the melting curves of fcc-Pd and bcc-Pd and the fcc–bcc solid–solid phase transition boundary leads us to conclude that (i) the initial slope of the fcc–bcc solid–solid phase transition boundary is ~ 23 K/GPa and (ii) the boundary is relatively flat. To further constrain the P–T location of this boundary, and to shed more light on the location of another solid–solid phase transition boundary on the phase diagram of Pd, namely, the rhcp–bcc one, we carried out two sets of inverse Z runs to determine which solid structure liquid Pd solidifies into. Since the solidification kinetics is approximately governed by the factor $\exp\{\Delta G/T_s\}$, where $\Delta G \equiv G_l - G_s$ is the difference between liquid and solid Gibbs total free energies at the solidification temperature T_s, in the case of several energetically competitive solid phases the most stable solid phase has the largest ΔG and must therefore be the fastest to solidify. Hence, the inverse Z method is expected to yield the most stable solid phase at a given (P, T).

Examples of the actual RDFs of fcc-Pd and bcc-Pd solidified from sc-based liquid with $a = 2.0$ Å can be found in the supplementary material (Figs. S1 and S2). The final states of the solidification of liquid Pd are shown in Fig. 10 as filled blue and green circles, respectively, for fcc and bcc, and a filled red circle for rhcp.

7. Analytic form of the fcc–bcc solid–solid phase transition boundary

A simple analytic form of the fcc–bcc solid–solid transition boundary which (i) crosses the triple point (P in GPa, T in K) $(P, T) = (106.6, 5452)$, (ii) has an initial slope of 23 K/GPa and (iii) takes into account the results of the inverse Z solidification simulations is

$$T(P) = 5452 + 23\,(P - 106.6) - 7.4\,(P - 106.6)^{1.17}. \tag{6}$$

The choice of this specific functional form is justified by its use in our previous studies on similar fcc–bcc solid–solid transition boundary in both Cu[12] and Ag[13] and is supported by the corresponding *ab initio* results. The phase boundary (6) is shown in Fig. 10.

The results of the previous section demonstrate that at the triple point the slope of the Pd melting curve increases slightly, by $\sim$15%, from 25.2 K/GPa on the fcc side to 29.1 K/GPa on the bcc side, similar to the case of Ag in which the change of slope at the fcc–bcc–liquid triple point is $\sim$10%.[13]

High-pressure polymorphism in Pd

Our cold enthalpy calculations (Fig. 2) imply that in the ~ 1.3–1.9 TPa P range another solid phase of Pd, in addition to fcc and bcc, can exist, namely, thcp or 9R, which are separated from each other by a mere 5 meV/atom. These two structures are typical examples of hexagonal polytypes, i.e., hexagonal structures which differ from each other by the staking sequence of the atomic layers: hcp (AB…), fcc (ABC…), dhcp (ABAC…), thcp (ABCACB…), 9R (ABCBCACAB…), etc. In this respect, the high-P polymorphism in Pd can be considered as a polytypism, i.e., a transition from one hexagonal polytype (fcc) to another (thcp or 9R). Typically, structures with different stacking sequences are energetically very close to each other; e.g., thcp and 9R in Fig. 2 are within 10 meV/atom. Hence, the energy cost of forming a stacking fault between two such structures is virtually zero. Consequently, the actual layer stacking could be non-periodic and, in principle, random. A randomly disordered hexagonal close-packed (rhcp) structure was hypothesized to be the high-PT physical phase of Pt[31] and/or Ir,[42] as well as the high-P solid phase of Ag at low T.[13] A structure similar to rhcp was conjectured to be the most stable solid phase of Fe at Earth's core PT conditions.[43] For the same reason, rhcp may find itself on the phase diagram of palladium.

8. The rhcp–bcc solid–solid phase transition boundary and the rhcp–fcc–bcc triple point

To shed more light on the issue of the existence of rhcp-Pd discussed above, we carried out a set of inverse-Z simulations using sc-based liquid with $a = 1.85$ Å which corresponds to a pressure of ∼1450 GPa. The RDF of the state solidified at 1500 K is shown in Fig. 8, and of those solidified at 3000, 4500, and 6000 K in Fig. 9. Although the RDFs shown in Fig. 9 clearly correspond to bcc, except perhaps that at 3000 K, the RDF of the state solidified at 1500 K is of hexagonal type. Figure 8 compares it to the RDFs of both (pure) fcc-Pd and hcp-Pd simulated at the same P-T conditions. It is clearly seen that, although this state has certain features of both fcc and hcp, e.g., the tallest peak at $R \sim 35$ of its RDF is identical to that of fcc while the peak at $R \sim 60$ is very similar to that of hcp, it is neither pure fcc nor pure hcp but rather their

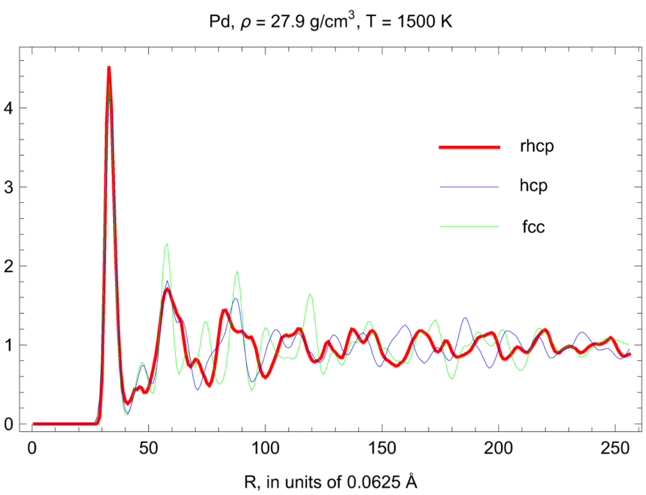

FIG. 8. RDFs of the final state of the solidification of liquid Pd at a pressure of ∼1450 GPa at $T = 1500$ K compared to those of both fcc-Pd and hcp-Pd simulated at the same P–T conditions.

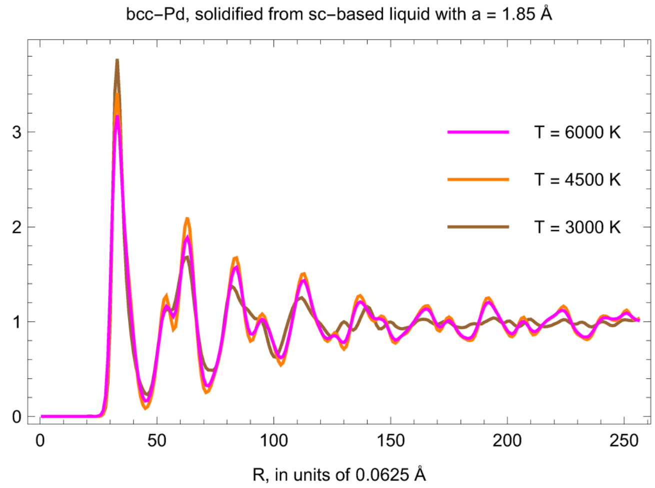

FIG. 9. RDFs of the final states of the solidification of liquid Pd at a pressure of ∼1450 GPa at higher temperatures.

mixture. In fact, its peak at $R \sim 80$ is virtually the average of those of fcc at $R \sim 75$ and hcp at $R \sim 85$. The exact RDF of rhcp is not known (e.g., it cannot be simulated with any existing code which uses periodic boundary conditions, such as VASP), but since rhcp is often assumed to be a mixture of fcc and hcp,[44] we tentatively assign the rhcp structure to the 1500 K state. As for the 3000 K state, its short-range order (smaller-R) peaks are definitely bcc-like, but its long-range order (larger-R) peaks are smeared, which may indicate a mixture with rhcp, or even with both fcc and rhcp. Thus, this state must be very close to the rhcp–bcc transition boundary, and perhaps to the rhcp–fcc–bcc triple point as well. Our tentative rhcp–fcc and rhcp–bcc solid–solid phase transition lines shown in Fig. 10 demonstrate exactly that.

Ab initio phase diagram of palladium

Now we combine all the results of the previous sections of this work to construct the theoretical *ab initio* phase diagram of palladium which is shown in Fig. 10.

Also shown in Fig. 10 is the Pd principal Hugoniot that we calculated theoretically,

$$T_{\mathrm{H}}(P) = 293 + 1.41 \times P^{1.54}. \tag{7}$$

It crosses the fcc–bcc phase transition boundary at $(P, T) = (225.0,\ 6202.5)$, which is our theoretical prediction. The Hugoniot melting point corresponds to the intersection of the bcc-Pd melting curve (4) and the above Hugoniot: $(P, T) = (318.3,\ 10377)$, which is also our theoretical prediction. This Hugoniot melting point is consistent with $\approx (340,\ 9400)$ of Ref. 14.

The solid–solid phase transition boundary (6) and the two melting curves (3) and (4) define the topology of our *ab initio* phase diagram of Pd shown in Fig. 10. This phase diagram looks similar to the *ab initio* phase diagram of Smirnov.[14] We note that the solution of the equation $T(P) = 0$ with $T(P)$ defined by (6) is

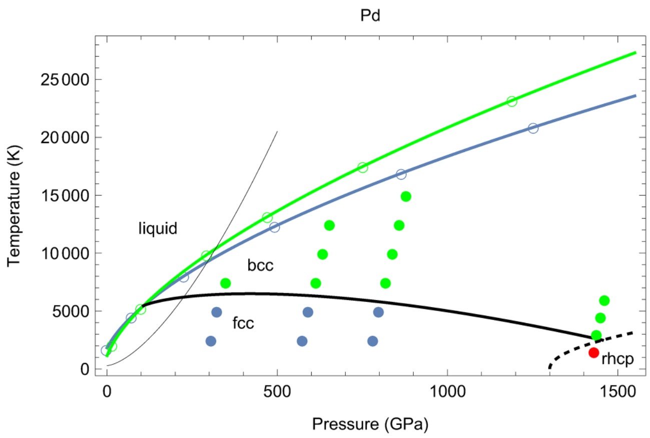

FIG. 10. The theoretical *ab initio* phase diagram of Pd to 1.5 TPa. The melting points as open circles, the final states of solidification as filled circles, and the melting curve as a solid line are shown in blue for fcc and in green for bcc. The fcc–bcc (solid black curve), and rhcp-fcc and rhcp-bcc (dashed black curve) solid–solid phase transition boundaries are calculated based on the results of the inverse Z method simulations. The theoretical melting curve of Pd is a combination of fcc and bcc segments, below and above the fcc–bcc–liquid triple point at ~100 GPa, respectively. The Pd principal Hugoniot is also shown as a thin black curve.

$P = 1806.7$ GPa ≈ 1.8 TPa, in agreement with the fcc–bcc transition point from our cold enthalpy calculations (Fig. 2). Thus, Eq. (6) can be considered at least as a good approximation for the actual fcc–bcc solid–solid phase transition boundary in the entire range of P that this phase boundary covers.

9. Topological similarity of the phase diagrams of palladium and silver

The phase diagram of palladium presented in this work and that of silver from Ref. 13 appear to be topologically similar, which is clearly seen from comparing Fig. 10 of this work and Fig. 5 of Ref. 13. It is well known that the phase diagrams themselves can be topologically similar (look-alike) or, in some cases, even topologically equivalent. The phase diagrams of Ti, Zr, and Hf are topologically similar; their only difference is in the slopes of the solid–solid transition boundaries between the three solid structures found on each of the three phase diagrams: hcp, hexagonal omega (hex-omega), and bcc. The phase diagrams of Si and Ge are topologically equivalent at low P: both contain semiconducting diamond and metallic tetragonal β-Sn solid structures, and the slopes of the corresponding solid–solid and solid–liquid phase boundaries are almost identical.[45] The topological equivalence of the phase diagrams of Mo and W is discussed in detail in Ref. 46, and the topological similarity of those of Ta and Nb was also noted.[47] In the case of Mo and W, the reason for their topological equivalence may be that the electronic wave functions of Mo and W and of their group 5B partner Cr are such that, with decreasing volume (increasing P), they become more spherically symmetric, which favors a higher atomic coordination number than 8 as that for bcc, their ambient solid phase and, correspondingly, a more symmetric structure than bcc. In both Mo and W the high-P structure appreas to be dhcp, while in Cr it is hcp.[48] In contrast Mo, W, and Cr, the electronic wave functions of V, Nb, and Ta are such that, with decreasing volume, they become less spherically symmetric, which favors a lower atomic coordination number than bcc's 8 and, correspondingly, a less symmetric structure than bcc, e.g., an orthorhombic one. This appears to be in agreement with the fact that, in both Nb[47] and Ta,[31] the high-P equilibrium solid structure is orthorhombic Pnma. In our case of Pd, the reason for the topological similarity of its phase diagram and that of Ag, its neighbor in the periodic table, may again be the electronic structure of both substances which may be responsible for basically identical interatomic interactions in either case. More specifically: the Coulombic origin of the pair-interaction term suggest the parametrization of pair interactions between atoms of types A and B in terms of the corresponding effective charges, $\phi_{AB}(R) = Z_A(R)\,Z_B(R)/R,$ where R is interatomic separatoin. As the detailed analysis of Ref. 34 shows, the effective charges of both Pd and Ag as functions of interatomic separation R are very close to each other and, in fact, virtually identical for $R > 4$ Å. Thus, the corresponding interatomic interactions are similar $\tilde{\text{to}}$ each other and must lead to the appearance of similar solid structures on the two phase diagrams and, as a result, to the two phase diagrams being similar to each other.

PALLADIUM AS A SHOCK STANDARD

Despite being polymorphic, Pd can be considered as a reliable SW standard. Indeed, (i) Pd is a plastic material, so that the characteristics of its both shock and static compression agree well with each other, (ii) when melted, Pd undergoes a minor volume change, so that its shock compression characteristics change very little across melting on the Hugoniot, and (iii) the SW characteristics of both fcc-Pd and bcc-Pd are expected to be virtually identical to each other. This is so because (i) the EOS parameters of both fcc-Pd and bcc-Pd listed under Eq. (1) are very similar; in particular, the two values of c differ from each other by 1.5% only while the two values of b are identical, and (ii) the volume change at the fcc–bcc solid–solid phase transition on the Hugoniot is also very minor, because in the vicinity of the Hugoniot transition point the fcc–bcc boundary is virtually flat ($dT/dP \approx 0$). Hence, in particular, T as a function of P along the Hugoniot should not change much across the fcc–bcc transition. This is why the Pd principal Hugoniot in the P-T coordinates, Eq. (7), discussed above can be used as a common $T_{\rm H}(P)$ for both fcc and bcc.

Here, we present the analytic form of the principal Hugoniot of Pd which can be used as a standard in shock compression experiments. It is given in the analytic framework established in our previous publications.[49,50] In this framework, a wide P range is divided into three regimes, and the Hugoniot is constructed in each of these regimes and then interpolated smoothly between them. These regimes are (i) the low-P regime in which the Hugoniot is described by $U_s = C + B\,U_p,$ where U_p and U_s are particle and shock velocities, respectively, and the values of C and B come from the experiment, (ii) the intermediate-P regime where the Hugoniot is described by the Thomas–Fermi–Kalitkin (TFK) model $U_s = c + b\,U_p + a\,U_p^2,$ with the values of $c,$ b and a determined virtually for all Zs, and (iii) the high-P regime in which the Hugoniot is described by the Debye-Hückel–Johnson (DHJ) model. The only assumption was made that the principal Hugoniot is governed by some function $U_s = U_s(U_p)$ (which is linear at low P and quadratic at intermediate P; its high-P form was established in[49]) and that this function is continuous and smooth (the first derivative dU_s/dU_p is continuous) at all U_p. Then it follows from the Rankine-Hugoniot (RH) relations[49] that compression ratio, pressure and internal energy are all continuous and smooth as well. No other assumption, and no additional free parameter except the six mentioned above, C, B, c, b, a, and Z, are required for the construction of the analytic model of the principal Hugoniot. In order to match the next regime, the linear form of the low-P regime is modified into $U_s = C + B\,U_p + A\,U_p^2$, where A is an additional, 7th, parameter which introduces a very small non-linearity ($A \sim 10^{-2}$ s/km) and is obtained using the formula $A = a - (B-b)^2/(4\,(c-C))$.[49]

10. Analytic model of principal Hugoniot

Here is a brief summary of the new analytic model, as per Ref. 49. The new model is based on the following representation of the shock velocity U_s as a function of the particle velocity U_p over the three U_p intervals which is continuous and smooth from one interval to the next,

$$U_s = C + B\,U_p + A\,U_p^2, \quad 0 \le U_p \le U_p^* = \frac{2(c-C)}{B-b}, \tag{8}$$

$$U_s = c + b\,U_p + a\,U_p^2, \quad U_p^* \le U_p \le U_p^{**}, \tag{9}$$

$$U_s = -\frac{d}{f} + \frac{4}{3}\,U_p + \frac{d\,U_p}{1+f\,U_p}, \quad U_p \ge U_p^{**}. \tag{10}$$

The corresponding expressions for P along the principal Hugoniot are

$$P = \frac{4\rho_0 C^2 \eta(\eta-1)}{\left\{\eta - B(\eta-1) + \sqrt{[\eta - B(\eta-1)]^2 - 4AC(\eta-1)^2}\right\}^2}, \quad 0 \le U_p \le U_p^*, \tag{11}$$

$$P = \frac{4\rho_0\,c^2\,\eta\,(\eta-1)}{\left\{\eta - b\,(\eta-1) + \sqrt{[\eta - b\,(\eta-1)]^2 - 4\,a\,c\,(\eta-1)^2}\right\}^2}, \quad U_p^* \le U_p \le U_p^{\max} = \sqrt{\frac{c}{a}}, \tag{12}$$

$$P = \frac{4\rho_0\,c^2\,\eta\,(\eta-1)}{\left\{\eta - b\,(\eta-1) - \sqrt{[\eta - b\,(\eta-1)]^2 - 4\,a\,c\,(\eta-1)^2}\right\}^2}, \quad U_p^{\max} \le U_p \le U_p^{**}, \tag{13}$$

$$P = \frac{\rho_0}{4f^2}\,\frac{\eta}{\eta-1}\left(\sqrt{12\,d\,\frac{\eta-1}{\eta-4}+1} - 1\right)^2, \quad U_p \ge U_p^{**}, \tag{14}$$

which define pressure along the Hugoniot as a continuous and smooth function of compression ratio $\eta \equiv \rho/\rho_0$, where ρ is density and the subscript 0 indicates the initial (unshocked) state.

In the above formulas, $0 \le U_p \le U_p^*$ corresponds to the low-P regime, and $U_p^{\max} \le U_p \le U_p^{**}$ and $U_p \ge U_p^{**}$ to the med-P and high-P regimes, respectively. The value of U_p^{**} is found from the equation[49]

$$\left[c + \left(b - \frac{4}{3}\right)U_p^{**} + a\,U_p^{**2}\right]^2 = L\left(b - \frac{4}{3} + 2\,a\,U_p^{**}\right). \tag{15}$$

Here $L \equiv 2/3\,E$, where $E = E_{\rm coh} + E_{\rm dis} + E_{\rm ion}$ is the sum of cohesive, dissociation and ionization energies in going from ambient T to $T \to \infty$.[49] Thus, $L = 2/3\,E \approx 2/3\,E_{\rm ion}$, since $E_{\rm ion} \gg E_{\rm coh}$ and $E_{\rm ion} \gg E_{\rm dis}$. The (very accurate) formula for L as a function of Z is[49]

$$L \approx \frac{875\,Z^{2.4}}{2\,Z + 0.006\,Z^2}\left(\frac{\rm km}{\rm s}\right)^2. \tag{16}$$

In these formulas for P, $U_p^* \le U_p \le U_p^{\max}$ and $U_p^{\max} \le U_p \le U_p^{**}$ correspond to the two sub-regimes of the med-P regime, namely, those below and above the turnaround point of $U_p^{\max} = \sqrt{c/a}$.[49] Here the turnaround point is the point of the maximum compression: at this point the $\eta = \eta(U_s)$ behavior changes from increasing with U_p to decreasing with U_p. It corresponds to $P_{\max} \equiv P(\eta_{\max}) \sim 1$–$10$ Gbar (10–100 TPa, or 0.1–1 PPa); typically, $P_{\max}$ increases with Z.

TABLE IV. Numerical values of the parameters for the analytic model of the principal Hugoniot for the Pd shock-wave standard.

Z	ρ_0	C	B	$A \times 10^2$	c	b	$a \times 10^5$	L	d	$f \times 10^3$	U_p^*	$U_p^{\max}$	U_p^{**}
46	12.00	4.016	1.525	−1.414 97	6.076 73	1.182 51	8.059 16	81 789.4	2.275 92	5.275 09	12.0339	274.5938	1198.93

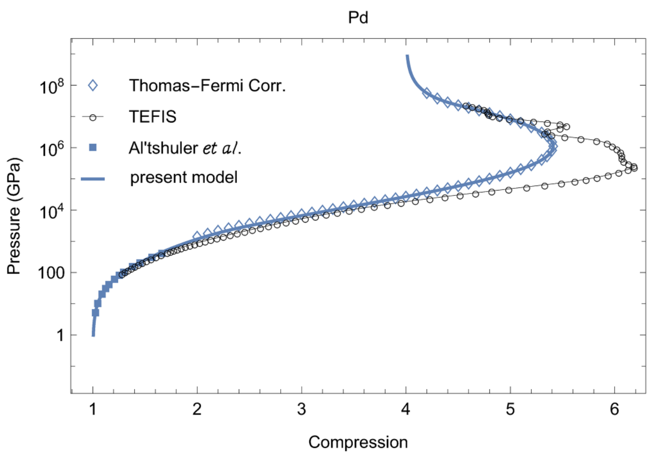

FIG. 11. The principal Hugoniot of Pd: our analytic form vs the theoretical results of Al'tshuler *et al.* of Ref. 51 (Al'tshuler *et al.*), the Pd Hugoniot from TEFIS database[54] (TEFIS) and our theoretical calculations using the Thomas-Fermi model with corrections (Thomas-Fermi Corr.).

11. Principal Hugoniot of Pd

Our calculations, using the methodology of,[49,50] result in the set of parameters for the Pd Hugoniot which are listed in Table IV.

Figure 11 compares the principal Hugoniot of Pd calculated using the analytic model of Refs. 49 and 50 with the parameters from Table IV to (i) the theoretical results of Al'tshuler *et al.* of Ref. 51, (ii) the Thomas-Fermi model with corrections (TFC),[52] and (iii) the Pd Hugoniot from TEFIS database.[53,54] For the TFC simulations, Lambert's orbital-free molecular dynamics (OFMD) code used, e.g., in a study on the transport properties of lithium hydride,[55] was modified appropriately. These simulations are similar to those of Ref. 56 for platinum. The (V, P) points that map out the Hugoniot (presented in the η-P coordinates upon conversion of the (V, P) points into the (η, P) ones) are found from the RH relation for internal energy: $E - E_0 = P(V_0 - V)/2$.

It is seen that our analytic form of the Pd principal Hugoniot is in excellent agreement with both the results of Ref. 51 and the TFC model, but is not consistent with the TEFIS Hugoniot at $\eta \gtrsim 4.5$. Possible reasons for the deviation of the TEFIS Hugoniots from the vast majority of the theoretical models were analyzed in Ref. 57 where it was concluded that this deviation may be the artifact of the interpolation scheme used for their construction. Specifically, this interpolation scheme is the scheme used in Refs. 58 and 59 for the interpolation between the portion of the Hugoniot below and across the turnaround point described by the TFK model and that above the turnaround point which incorporates electron shell effects; such shell effects are clearly seen in Fig. 11 in the vicinity of the turnaround point.

CONCLUDING REMARKS

Let us now summarize the results of our combined experimental and theoretical study on the phase diagram of palladium.

On the experimental side, we have obtained the EOS of fcc-Pd to 80 GPa and the corresponding XRD patterns at selected *P*s which are shown in Fig. 1. On the theoretical side, we have constructed the phase diagram of Pd to 1.5 TPa, using a suite of *ab initio* QMD simulations based on the Z methodology which combines both the simulation of melting curves using direct Z method and the calculation of solid–solid phase boundaries using inverse Z method. We determined that the phase diagram of Pd contains another two solid phases, bcc and rhcp, in addition to fcc, its solid phase at ambient conditions. We have calculated the melting curves of both fcc-Pd and bcc-Pd, determined the location of the fcc–bcc–liquid triple point, and obtained an equation for the fcc–bcc solid–solid phase transition boundary. We also estimated the location of the rhcp-fcc and rhcp-bcc solid–solid phase transition boundaries at low T and TPa pressures, and the rhcp–fcc–bcc triple point. Further refinement of this theoretical phase diagram, including its extension beyond 1.5 TPa and the more accurate determination of the rhcp–bcc transition boundary will be the subject of our subsequent studies.

The thermal EOSs for both fcc-Pd and bcc-Pd that we presented in this work appear to be in agreement with both experimental data and QMD simulations. Our theoretical phase diagram of Pd can be considered as the refinement of that by Smirnov[14] as it extends the latter to much higher P and incorporates another solid phase of Pd, namely, rhcp.

We have also presented the analytic model of the Pd principal Hugoniot which may serve as a standard for experimental shock-compression studies.

SUPPLEMENTARY MATERIAL

This section contains atomic volume of fcc-Pd as a function of pressure in our experimental study described in the main text (Table S1), the results of convergence test: dependence of both energy per atom (E) and pressure (P) on the cutoff energy (ENCUT) for a fcc-Pd unit cell with a lattice constant of 2.86 Å simulated using a $60 \times 60 \times 60$ k-point mesh (Table S2), comparison of the $T = 300$ K equations of state of Refs. 2, 8 and 9 to the $T = 0$ one presented in this work (Table S3), RDFs of the final states of the solidification of liquid Pd at a pressure of ~ 600 GPa at lower temperatures of 2500 and 5000 K (Fig. S1), RDFs of the final states of the solidification of liquid Pd at a pressure of ~ 600 GPa at higher temperatures of 7500, 10 000, and 12 500 K (Fig. S2).

ACKNOWLEDGMENTS

This work was done under the auspices of the US DOE/NNSA. The QMD simulations were performed on the LANL cluster Badger as part of both the Institutional Computing projects w22_phadiagractox and w22_phadiatitial. D. E. acknowledges financial support from Spanish Ministerio de Ciencia, Innovación y Universidades (Grants Nos. PID2019-106383GB-C41 and RED2018-102612-T), and Generalitat Valenciana (PROMETEO CIPROM/2021/075-GREENMAT and MFA/2022/007). S.A. thanks the Generalitat Valenciana for the postdoctoral fellowship CIDEXG/2022/6.

AUTHOR DECLARATIONS

Conflict of Interest

The authors have no conflicts to disclose.

Author Contributions

S. R. Baty: Investigation (equal); Writing – review & editing (equal). **L. Burakovsky:** Investigation (equal); Methodology (equal); Writing – original draft (lead); Writing – review & editing (equal). **D. J. Luscher:** Funding acquisition (equal); Project administration (equal); Supervision (equal); Writing – review & editing (equal). **S. Anzellini:** Investigation (equal); Project administration (equal); Resources (equal); Writing – review & editing (equal). **D. Errandonea:** Funding acquisition (equal); Investigation (equal); Supervision (equal); Writing – review & editing (equal).

DATA AVAILABILITY

The data that support the findings of this study are available from the corresponding author upon reasonable request.

REFERENCES

[1] D. G. Narehood *et al.*, "X-ray diffraction and H-storage in ultra-small palladium particles," Int. J. Hydrogen Energy **34**, 952 (2009).
[2] B. Guigue, G. Geneste, B. Leridon, and P. Loubeyre, "An x-ray study of palladium hydrides up to 100 GPa: Synthesis and isotopic effects," J. Appl. Phys. **127**, 075901 (2020).
[3] R. J. Miller and C. B. Satterthwaite, "Electronic model for the reverse isotope effect in superconducting Pd-H(D)," Phys. Rev. Lett. **34**, 144 (1975).
[4] C. Cogran and G. Pottlacher, "Thermophysical properties of palladium," Platin. Met. Rev. **50**, 144 (2006).
[5] N. Milošević and M. Babić, "Thermophysical properties of solid phase palladium over a wide temperature range," Int. J. Mater. Res. **104**, 5 (2013).
[6] J. W. Arblaster, "A re-assessment of the thermodynamic properties of palladium," Johnson Matthey Technol. Rev. **62**, 48 (2018).
[7] H. K. Mao, P. M. Bell, J. T. Shaner, and D. J. Steinberg, "Specific volume measurements of Cu, Mo, Pd, and Ag and calibration of the ruby R_1 fluorescence pressure gauge from 0.06 to 1 Mbar," J. Appl. Phys. **49**, 3276 (1978).
[8] T. Fedotenko *et al.*, "Synthesis of palladium carbides and palladium hydride in laser heated diamond anvil cells," J. Alloys Comp. **844**, 156179 (2020).
[9] M. Frost, D. Smith, E. E. McBride, J. S. Smith, and S. H. Glenzer, "The equations of state of statically compressed palladium and rhodium," J. Appl. Phys. **134**, 035901 (2023).
[10] Z.-T. Liu *et al.*, "Phase transitions of palladium under dynamic shock compression," Acta Phys. Sin. **71**, 037102 (2022).
[11] N. A. Smirnov, "Relative stability of Cu, Ag, and Pt at high pressures and temperatures from *ab initio* calculations," Phys. Rev. B **103**, 064107 (2021).
[12] S. R. Baty, L. Burakovsky, and D. Errandonea, "*Ab initio* phase diagram of copper," Crystals **11**, 537 (2021).
[13] S. R. Baty, L. Burakovsky, and D. Errandonea, "*Ab initio* phase diagram of silver," J. Phys.: Condens. Matter **33**, 485901 (2021).
[14] N. A. Smirnov, "*Ab initio* calculations of structural stability, thermodynamic and elastic properties of Ni, Pd, Rh, and Ir at high pressures," J. Appl. Phys. **134**, 025901 (2023).
[15] D. Errandonea, "High-pressure melting curves of the transition metals Cu, Ni, Pd, and Pt," Phys. Rev. B **87**, 154108 (2013).
[16] J.-W. Jeong and K. J. Chang, "Molecular-dynamics simulations for the shock hugoniot meltings of Cu, Pd and Pt," J. Phys.: Condens. Matter **11**, 3799 (1999).
[17] Z.-L. Liu, J. H. Yang, L. C. Cai, F. Q. Jing, and D. Alfe, "Structural and thermodynamic properties of compressed palladium: *Ab initio* and molecular dynamics study," Phys. Rev. B **83**, 144113 (2011).
[18] B. Zhang, B. Wang, and Q. Liu, "Melting curves of Cu, Pt, Pd and Au under high pressures," Int. J. Modern Phys. B **30**, 1650013 (2016).
[19] N. Q. Hoc, T. D. Cuong, B. D. Tinh, and L. H. Viet, "High-pressure melting curves of FCC metals Ni, Pd and Pt with defects," Modern Phys. Lett. B **33**, 1950300 (2019).
[20] A. Dewaele, P. Loubeyre, and M. Mezouar, "Equations of state of six metals above 94 GPa," Phys. Rev. B **70**, 094112 (2004).
[21] S. Anzellini *et al.*, "Laser-heating system for high-pressure x-ray diffraction at the extreme conditions beamline I15 at diamond light source," J. Synchrotron Rad. **25**, 1860 (2018).
[22] C. Prescher and V. B. Prakapenka, "*DIOPTAS*: A program for reduction of two-dimensional x-ray diffraction data and data exploration," High Pressure Res. **35**, 223 (2015).
[23] A. A. Coelho, "TOPAS and TOPAS-academic: An optimization program integrating computer algebra and crystallographic objects written in C++," J. Appl. Crystallogr. **51**, 210 (2018).
[24] G. Kresse and J. Furthmüller, "Efficiency of *ab initio* total energy calculations for metals and semiconductors using a plane-wave basis set," Comput. Mater. Sci. **6**, 15 (1996).
[25] G. Kresse and J. Furthmüller, "Efficient iterative schemes for *ab initio* total-energy calculations using a plane-wave basis set," Phys. Rev. B **54**, 11169 (1996).
[26] J. P. Perdew *et al.*, "Restoring the density-gradient expansion for exchange in solids and surfaces," Phys. Rev. Lett. **100**, 136406 (2008).
[27] A. Dewaele, M. Torrent, P. Loubeyre, and M. Mezouar, "Compression curves of transition metals in the Mbar range: Experiments and projector augmented-wave calculations," Phys. Rev. B **78**, 104102 (2008).
[28] L. Dubrovinsky *et al.*, "Noblest of all metals is structurally unstable at high pressure," Phys. Rev. Lett. **98**, 045503 (2007).
[29] Georg Kresse (Vienna), private communication (2017).
[30] A. B. Belonoshko, N. V. Skorodumova, A. Rosengren, and B. Johansson, "Melting and critical superheating," Phys. Rev. B **73**, 012201 (2006).
[31] L. Burakovsky, S. P. Chen. D.L. Preston, and D. G. Sheppard, "Z methodology for phase diagram studies: Platinum and tantalum as examples," J. Phys. Conf. Ser. **500**, 162001 (2014).
[32] L. Burakovsky, N. Burakovsky, and D. L. Preston, "*Ab initio* melting curve of osmium," Phys. Rev. B **92**, 174105 (2015).
[33] J. W. Arblaster, "Crystallographic properties of palladium," Platin. Met. Rev. **56**, 181 (2012).
[34] S. M. Foiles, M. I. Baskes, and M. S. Daw, "Embedded-atom-method functions for the FCC metals Cu, Ag, Au, Ni, Pd, Pt, and their alloys," Phys. Rev. B **33**, 7983 (1986).
[35] J. A. Rayne, "Elastic constants of palladium from 4.2–300°K," Phys. Rev. **118**, 1545 (1960).
[36] D. K. Hsu and R. G. Leisure, "Elastic constants of palladium and β-phase palladium hydride between 4 and 300 K," Phys. Rev. B **20**, 1339 (1979).
[37] A. B. Belonoshko, J. Fu, and G. Smirnov, "Free energies of iron phases at high pressure and temperature: Molecular dynamics study," Phys. Rev. B **104**, 104103 (2021); *ibid.* erratum— **105**, 159903 (2022).
[38] T. Górecki, "Vacancies and a generalised melting curve of metals," High Temp. High Pressure **11**, 683 (1979).
[39] S. V. Stankus and P. V. Tyagelsky, "Thermal properties of palladium in the temperature range 293–2250 K," Teplofiz. Vysokikh Temp. **30**, 188 (1992).
[40] G. Kaptay, "Approximated equations for molar volume of pure solid fcc metals and their liquids from zero Kelvin to above their melting points at standard pressure," J. Mater. Sci. **50**, 678 (2015).
[41] C. Pu, X. Yang, D. Xiao, and J. Cheng, "Molecular dynamics simulations of shock melting in single crystal Al and Cu along the principle hugoniot," Mater. Today Commun. **26**, 101990 (2021).

[42]L. Burakovsky, N. Burakovsky, M. J. Cawkwell, D. L. Preston, D. Errandonea, and S. I. Simak, "*Ab initio* phase diagram of iridium," Phys. Rev. B **94**, 094112 (2016).
[43]T. Ishikawa, T. Tsuchiya, and J. Tsuchiya, "Stacking-disordered phase of iron in the Earth's inner core from first principles," Phys. Rev. B **83**, 212101 (2011).
[44]P. Krishna and A. R. Verma, "Crystal-polymorphism in one dimension," Phys. Status Solidi **17**, 437 (1966).
[45]L. Burakovsky and D. L. Preston, "Shear moduli of silicon and germanium in semiconducting and metallic phases," Defect Diffus. Forum **210–212**, 43 (2002).
[46]S. Baty, L. Burakovsky, and D. L. Preston, "Topological equivalence of the phase diagrams of molybdenum and tungsten," Crystals **10**, 20 (2020).
[47]D. Errandonea *et al.*, "Experimental and theoretical confirmation of an orthorhombic phase transition in niobium at high pressure and temperature," Commun. Mater. **1**, 60 (2020).
[48]S. R. Baty, L. Burakovsky, D. J. Luscher, S. K. Sjue, and D. Errandonea, "*Ab initio* phase diagram of chromium to 2.5 TPa," Appl. Sci. **12**, 7844 (2022).
[49]L. Burakovsky, D. L. Preston, S. D. Ramsey, and R. S. Baty, "Analytic model of principal hugoniot at all pressures," J. Appl. Phys. **132**, 215109 (2022).
[50]L. Burakovsky, D. L. Preston, S. D. Ramsey, and R. S. Baty, "Shock standards Cu, Ag, Ir, and Pt in a wide pressure range," Matter Radiat. Extremes **8**, 046901 (2023).
[51]L. V. Al'tshuler, S. E. Brusnikin, and E. A. Kuz'menkov, "Isotherms and Grüneisen functions for 25 metals," J. Appl. Mech. Tech. Phys. **28**, 134 (1987).
[52]V. P. Kopyshev, Equations of State Theory (Sarov: RFNC- VNIIEF, 2009) [in Russian]; see also Nikiforov, A. F.; Novikov, V. G.; Uvarov, V. B.; Quantum-Statistical Models of Hot Dense Matter. Methods for Computation Opacity and Equation of State (Basel, Birkhäuser, 2005).
[53]E. S. Ivanchenko, N. N. Kalitkin, and L. V. Kuz'mina, "Main hugoniot adiabats in the TEFIS database of thermophysical properties of substances (TEFIS)," Math. Models Comput. Simul. **1**, 383 (2009).
[54]A. A. Belov *et al.*, TEFIS database. Thermodynamic properties of substances, Keldysh IAM Preprint 219 (2018), https://keldysh.ru/papers/2018/prep2018_219.pdf.
[55]L. Burakovsky, C. Ticknor, J. D. Kress, L. A. Collins, and F. Lambert, "Transport properties of lithium hydride at extreme conditions from orbital-free molecular dynamics," Phys. Rev. E **87**, 023104 (2013).
[56]V. M. Elkin, V. N. Mikhaylov, A. A. Ovechkin, and N. A. Smirnov, "A wide-range multiphase equation of state for platinum," J. Phys. Condens. Matter **32**, 435403 (2020).
[57]L. Burakovsky, D. L. Preston, S. D. Ramsey, S. K. Sjue, C. E. Starrett, and R. S. Baty, "Principal hugoniots of promethium, terbium, thulium, lutetium, and actinium in a wide pressure range," Appl. Sci. **13**(17), 9643 (2023).
[58]E. S. Ivanchenko, N. N. Kalitkin, and L. V. Kuzmina, "Quantum-statistical calculations of thermodynamics and hugoniots (codes QSM)," Math. Model. **20**, 30 (2008).
[59]E. S. Ivanchenko and N. N. Kalitkin, "Shock wave data interpretation in the TEFIS database," Math. Models Comput. Simul. **2**, 526 (2010).